Journal of Materials Chemistry C

ROYAL SOCIETY OF CHEMISTRY

PAPER

Published on 10 November 2025
Licensed under CC-BY 4.0

Check for updates

Cite this: J. Mater. Chem. C, 2026, 14, 1145

Alloying Au into a Cu/Cu_2O/nickel foam photoanode for solar-enhanced hydrogen production coupled with glucose oxidation

Chinh Chien Nguyen,*[ab] To Luong Nguyen,[c] Do Thi Thuy Van,[c] Trung Hieu Le,[d] Lam Son Le,[d] Minh Tuan Nguyen Dinh,[e] Thi Van Thi Tran,[d] Nguyen Dang Giang Chau,[d] Thi Hong Chuong Nguyen,[ab] Anh Tuyen Luu,[f] Ekaterina Korneeva,[g] Nguyen Van Tiep,[h] My Uyen Dao,[ab] Minh Khoa Duong[i] and Trong-On Do*[i]

The Cu/Cu_2O photoelectrocatalyst, possessing strong active centers and a narrow bandgap, has been considered a potential photoanode for photoelectrocatalytic hydrogen production coupled with glucose oxidation. However, its limited charge separation and solar utilization capability have been considered as bottleneck issues, restricting its performance. Herein, a novel $Au/Cu/Cu_2O$-decorated nickel foam (denoted as Au–Cu/NF) was tailored as a photoanode for the photoelectrocatalytic hydrogen production-coupled glucose oxidation reaction (Pe-GOR). This material was prepared *via* a glycerol-assisted hydrothermal method, resulting in the alloying of Au atoms into the Cu/Cu_2O/NF structure. The employed characterizations unveil the alloying of Au atoms into the structure *via* the formation of an Au–Cu alloy on the NF support through intimate linkages (*e.g.*, Au–Cu–Ni), which unambiguously promotes solar light absorption and charge transport capabilities. Consequently, the Au–Cu/NF sample exhibits outstanding photoelectrocatalytic activity and stability in the Pe-GOR. Notably, the achieved Au–Cu/NF photoanode produces an average of 2.57 mmol H_2 h^{-1} cm_{geo}^{-2} at 1.62 V *vs.* RHE for 15 cycles within a total working time of 45 hours. The presented material demonstrates a novel strategy toward the utilization of photoelectrocatalysts for the solar-enhanced hydrogen production-coupled glucose oxidation reaction.

Received 3rd August 2025, Accepted 9th November 2025

DOI: 10.1039/d5tc02936h

rsc.li/materials-c

1. Introduction

Green hydrogen has been considered a crucial factor in decarbonizing hard-to-electrify sectors on the pathway to the 2050 climate target.[1,2] Indeed, this energy carrier offers three features, as follows: (i) high gravimetric energy density; (ii) potential for production *via* a low carbon-footprint pathway; and (iii) suitability as a promising candidate for the transition of heavy industries.[3] For these reasons, policymakers have made numerous attempts to stimulate the green hydrogen market.[4] However, high production costs are considered the primary obstacle, limiting the deployment of green hydrogen on a large scale.[5]

The utilization of alkaline electrolyzers has been considered a viable tactic for large-scale hydrogen production. However, the high overpotential of the anodic oxygen evolution reaction (OER) has been regarded as the primary problem, causing high energy consumption, which leads to a high production cost.[6] To address the mentioned issue, electrocatalytic hydrogen production integrated with the glucose oxidation reaction (GOR) has garnered increasing attention, as it enables the replacement of the OER with the GOR, which occurs at a significantly lower potential. Moreover, the formation of value-added products (*e.g.*, gluconic acid) is considered a positive aspect, offering alternative pathways to produce valuable molecules.[7]

[a] Center for Advanced Chemistry, Institute of Research and Development, Duy Tan University, Danang, 550000, Vietnam. E-mail: nguyenchinhchien@duytan.edu.vn
[b] Faculty of Natural Sciences, Duy Tan University, Danang, 550000, Vietnam
[c] Faculty of Physics and Chemistry, The University of Danang - University of Science and Education, Danang 550000, Vietnam
[d] Faculty of Chemistry, Hue University of Sciences, Hue University, Thua Thien Hue 530000, Vietnam
[e] The University of Danang – University of Science and Technology, Danang 550000, Vietnam
[f] Center for Nuclear Technologies, Vietnam Atomic Energy Institute, Ho Chi Minh City, 700000, Vietnam
[g] Flerov Laboratory of Nulear Reactions, Joint Insititute for Nuclear Research, 141980 Dubna, Moscow Reg., Russia
[h] Institute of Physics, Vietnam Academy of Science and Technology, 10 Dao Tan, Ba Dinh, Hanoi 10000, Vietnam
[i] Department of Chemical Engineering, Laval University, 1065 Avenue de la Médecine, Quebec, Quebec G1 V0A6, Canada. E-mail: Trong-On.Do@gch.ulaval.ca

However, the overall energy consumption associated with glucose oxidation and hydrogen production remains high.[8] Therefore, developing a high-performance system is essential.

The employment of a photoelectrocatalytic system has emerged as a potential strategy for hydrogen production coupled with glucose oxidation.[9–11] This approach involves the utilization of a photoanode that not only functions as an electrocatalyst but also exploits solar energy to produce electron–hole pairs for the hydrogen evolution reaction (HER) and GOR, respectively. As a result, such a configuration can improve the hydrogen production activity compared to that of the GOR counterpart. Consequently, the development of an anodic material that not only possesses electrocatalytic features (*e.g.*, robust active centers and low charge-transfer resistance) but also contains efficient solar light absorption and promotes charge separation is highly desirable.

Cu/Cu_2O-based catalysts have garnered attention because of their outstanding electrocatalytic properties for hydrogen production integrated with glucose oxidation. Such a catalytic architecture thus offers numerous active sites and promotes charge transportation.[12–14] Moreover, Cu/Cu_2O catalysts exhibit broad light absorption due to the narrow bandgap of Cu_2O of approximately 2.17 eV, suggesting their potential as a promising hierarchical structure for the solar-light-assisted glucose oxidation reaction.[15–17] However, their weak solar absorption capability and fast charge recombination are considered bottleneck issues, restricting the utilization of Cu/Cu_2O-based catalysts in photoelectrocatalytic glucose oxidation. For these reasons, the development of a novel Cu/Cu_2O-based photoelectrocatalyst that exhibits outstanding light absorption and charge separation properties may open a new avenue for hydrogen production coupled with glucose oxidation.

Inspired by the aforementioned obstacles, we herein present the exploration of a novel Au/Cu/Cu_2O-decorated nickel foam (denoted as Au–Cu/NF) photoelectrocatalyst synthesized *via* a facile hydrothermal method. The achieved Au–Cu/NF exhibits strong solar light absorption and boosted charge transport. The employed characterizations unveil the formation of a unique architecture within the obtained Au–Cu/NF structure, in which the Au–Cu alloy is formed and anchored onto the NF support. Such a structural configuration is considered the primary reason contributing to the boosted photoelectrocatalytic activity. The achieved material thus offers a novel route toward solar-driven hydrogen production *via* glucose oxidation. Consequently, the Au–Cu/NF photoelectrode demonstrates outstanding photoelectrocatalytic glucose oxidation (Pe-GOR) performance and impressive stability.

2. Results and discussions

The synthesis of the Au–Cu/NF photoelectrocatalyst involved the participation of Cu^{2+}, $AuCl_4^-$, glycerol, and nickel foam (NF) precursors, which were subjected to a hydrothermal treatment at 160 °C, as presented in Fig. 1A. The detailed synthesis is described in the Experimental section (see the SI). Fig. 1B–D

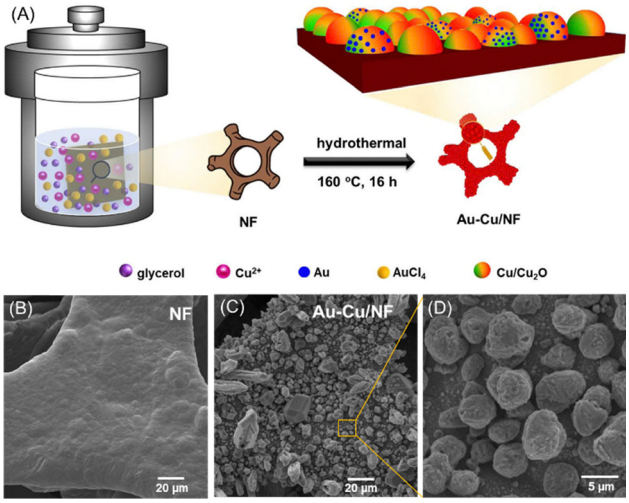

Fig. 1 Illustration of the preparation of the Au–Cu/NF sample (A) and SEM images of the as-prepared NF (B) and Au–Cu/NF (C) and (D).

display the scanning electron microscopy (SEM) images of the samples before and after hydrothermal treatment, suggesting the successful decoration of heteroparticles onto the NF support.

Further characterizations were conducted to unveil the structural properties of the synthesized Au–Cu/NF materials. Fig. 2A exhibits the X-ray diffraction (XRD) patterns of the obtained samples. All the obtained materials show two notable peaks centered at 44.5° and 51.8°, which can be attributed to the (111) and (200) planes of metallic Ni (JCPDS no. 04-0850), respectively.[18,19] The XRD patterns of both Au–Cu/NF and Cu/NF catalysts exhibit the characteristics of Cu phases (*i.e.*, 2θ = 43.4° and 50.5°) and Cu_2O phases (*i.e.*, 2θ = 29.5°, 36.6°, 42.4°, and 61.57°).[20–24] Moreover, no diffraction peaks corresponding to Au species are detected in the Au–Cu/NF sample, which may be due to their low concentration and ultrasmall size.

UV-Vis spectroscopy was employed to investigate the optical properties of the prepared samples, as shown in Fig. 2B. The bare NF exhibits weak light absorption, which is attributed to its metallic nature. The as-prepared Cu/NF catalyst exhibits the absorption edge at 650 nm, which can be assigned to the absorption of the Cu_2O component.[25–27] The weak absorption band in the range of 650–750 nm can be attributed to the d–d transitions of Cu(II), suggesting the presence of a trace level of CuO.[28–30] The Au–Cu/NF catalyst shows a distinct absorption profile compared to the NF and Cu/NF samples, with enhanced light absorption. Furthermore, a notable absorption edge of approximately 450 nm arises, whereas the CuO-derived signal disappears. This evidence indicates more efficient utilization of solar light and the formation of an extra component due to the incorporation of Au species in the Au–Cu/NF sample.

X-ray photoelectron spectroscopy (XPS) was employed to investigate the chemical oxidation states of elements in the prepared materials. As shown in Fig. S2, the XPS survey spectrum confirms the existence of Ni, Cu, O, and Au in the prepared Au–Cu/NF. The atomic amount of Au is estimated to

 This journal is © The Royal Society of Chemistry 2026

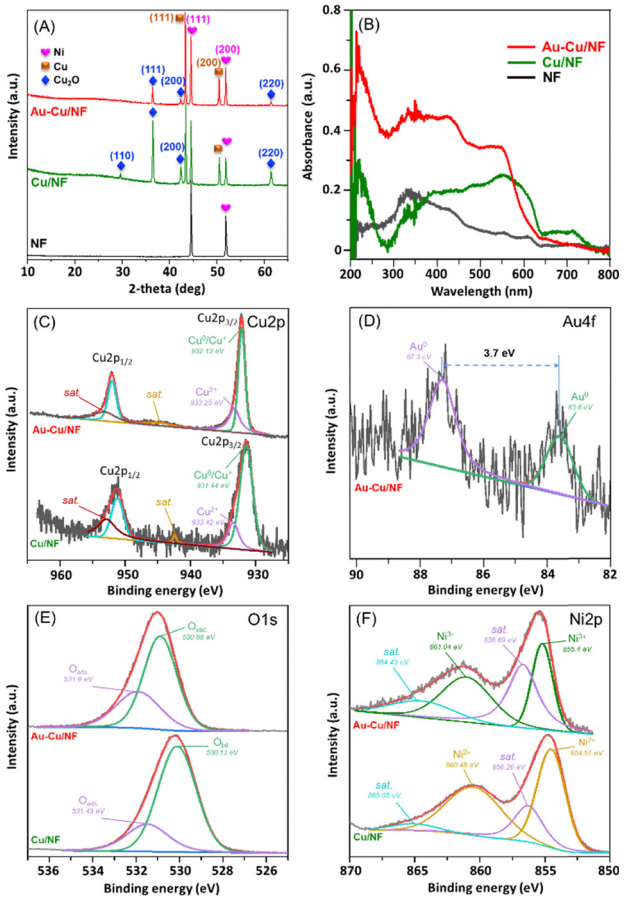

Fig. 2 XRD spectra (A); UV-Vis spectra (B); and XPS spectra of Cu 2p (C), Au 4f (D), O 1s (E), and Ni 2p (F) of the as-prepared samples.

be 0.12% (Table S1). Fig. 2C exhibits the deconvoluted Cu 2p spectra of the samples with and without Au incorporation. The Cu $2p_{3/2}$ spectrum of the Cu/NF sample shows two peaks centered at 931.44 and 933.42 eV, which can be attributed to the Cu(0)/Cu(I) and Cu(II) states, respectively.[31] Meanwhile, the Cu $2p_{3/2}$ spectrum of Au–Cu/NF shows a peak centered at 932.15 eV, which is higher than that of the Cu/NF counterpart. This shift implies a lower electron density surrounding Cu atoms.[32] As shown in Fig. 2D, the Au XPS spectrum is deconvoluted into two peaks centered at binding energies of 87.3 and 83.6 eV, which are lower than those of the reported metallic Au state (~84.0 and ~87.8 eV, respectively).[33] These observations, which can be made for Au–Cu alloy-based systems, originate from the electronegativity difference between Au (2.54) and Cu (1.90), resulting in the electron transfer from Cu to Au atoms.[34–37] As shown in Fig. 2E, the two peaks located at 530.88 and 531.9 eV in the deconvoluted O1s XPS spectrum of Au–Cu/NF can be assigned to the oxygen vacancies and adsorbed water molecules, respectively.[12,38,39] These peaks are found to be at higher binding energies than those of the Cu/NF sample, suggesting a decrease in the electron density surrounding the O atoms.

The high-resolution Ni 2p XPS spectrum of the Cu/NF material consists of two peaks centered at 854.51 and 860.48 eV, assigned to the Ni^{2+} oxidation state, as shown in Fig. 2F.[40,41] In contrast, the Au–Cu/NF sample exhibits peaks located at 855.4 and 861.04 eV, which are attributed to Ni^{3+} species.[40,41] Therefore, the XPS analysis provides two essential insights into the Au–Cu/NF structure, as follows: (i) the introduction of Au species can produce an additional AuCu alloy component in addition to the existing Cu and Cu_2O constituents, which is consistent with the UV-Vis results, and (ii) the possible formation of a direct interaction of Au and Cu atoms with the Ni support, inducing changes in the electron density surrounding all involved elements.

Fig. 3A–E show the TEM analysis of the prepared Au–Cu/NF electrocatalyst. The TEM image and corresponding elemental mapping signify the homogeneous distribution of the Ni, Cu, O, and Au atoms in the prepared samples, indicating the possibility of Cu–Au alloy formation. Moreover, selective area electron diffraction (SAED) reveals *d*-spacings of 0.218 and 0.190 nm, which can be attributed to the (111) and (200) planes of the Cu–Au alloy, respectively, as shown in Fig. 3F.[42–44] The high-resolution TEM (HR-TEM) image reveals the lattice fringes of 0.245 and 0.220 nm, corresponding to the (111) and (200) facets of Cu_2O, respectively.[45,46] In addition, the *d*-spacing of 0.218 nm, which is higher than that of Cu (111) (*i.e.*, 0.208 nm), can be assigned to the (111) plane of Cu–Au (Fig. 3G).[47] As shown in Fig. S3, the EDX spectrum further confirms the presence of Ni, Cu, and Au elements in the as-prepared sample. The detection of both Au and Cu indicates the successful incorporation of Cu and Au in the alloy structure, consistent with HR-TEM and SAED analyses.

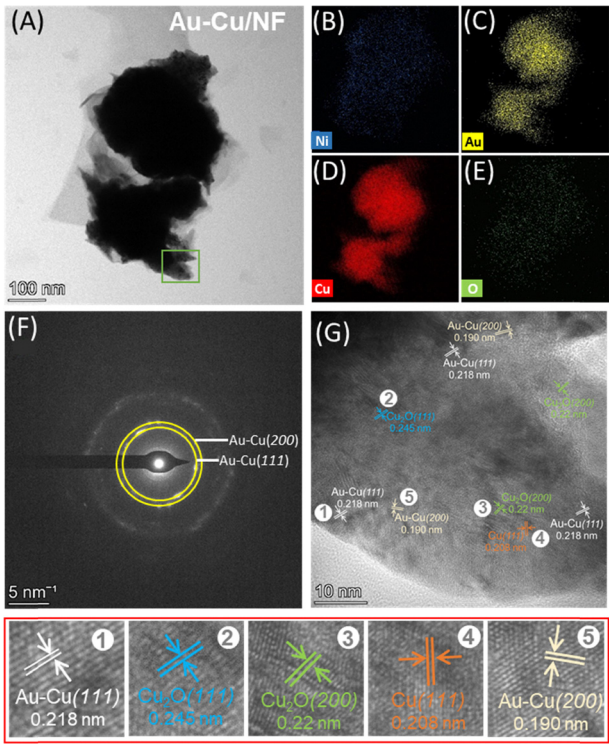

Fig. 3 TEM image (A), corresponding elemental mapping images (B)–(E), SAED pattern (F) and HR-TEM image (G) of the Au–Cu/NF sample.

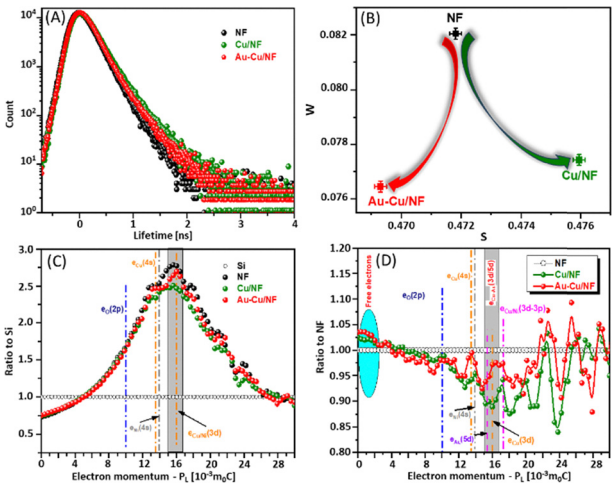

Fig. 4 PAL spectra (A). Correlation plots for S and W parameters of DB measurements (B). EMD spectra obtained using single-crystal silicon (C) and a NF (D) as references.

To gain fundamental insights into the nature of defects and interfacial interactions within the samples, positron annihilation lifetime spectroscopy (PALS), Doppler broadening (DB), and electron momentum distribution (EMD) analyses were conducted, as shown in Fig. 4 and Table 1.[13,48,49] The PALS results reveal two distinct positron lifetime components, where τ_1 corresponds to positron annihilation in mono-vacancies and τ_2 reflects annihilation in vacancy clusters, as shown in Fig. 4A.[13] Compared to the bare NF, the τ_1 value slightly increases upon Cu loading on the NF, while the I_1 intensity significantly decreases, indicating the generation of additional mono-vacancies due to Cu introduction. In contrast, the incorporation of Au leads to a notable reduction in τ_1 and a recovery of I_1, suggesting that Au atoms play a key role in reducing vacancy-type defects by promoting the atomic ordering or alloying-induced passivation of pre-existing defects. This behavior implies that the presence of Au may suppress surface Ni corrosion and, consequently, hinder the generation of mono-vacancies, likely through stabilizing interactions between Au and Cu atoms on the NF. These interactions not only protect the Ni surface but also modulate the defect landscape through controlled alloy formation.

The DB spectroscopy results further confirm the changes in the electronic structure and defect chemistry (Fig. 4B). The S parameter reflects the annihilation of positrons with low-momentum valence electrons and is typically sensitive to the defect concentration. Meanwhile, the W parameter corresponds to annihilation with high-momentum core electrons and is indicative of changes in the chemical environment surrounding the annihilation sites.[50] For the Cu/NF sample, the S value increases relative to the NF, implying enhanced positron trapping at valence-electron-rich defect sites, which is consistent with the PALS result indicating an increase in mono-vacancies. However, upon the incorporation of Au, the S value drops below that of the NF, indicating a reduction in defect-induced positron trapping and a more ordered atomic environment. Simultaneously, the W parameter shows a steady decrease from the NF to Cu/NF and further to Au–Cu/NF, reflecting a progressive alteration in the chemical surroundings at the annihilation sites, likely due to Au–Cu–Ni alloy formation and the redistribution of the core electron density.

Table 1 Positron annihilation lifetimes and intensities obtained from PAL measurements and values of the two characteristic S and W parameters obtained from DB measurements

Samples	τ_1 [ns]	τ_2 [ns]	I_1 [%]	I_2 [%]	S	W
NF	0.162	0.329	86.9	13.1	0.472	0.082
Cu/NF	0.167	0.338	73.3	26.7	0.476	0.077
Au–Cu/NF	0.145	0.326	77.3	22.7	0.469	0.076

These findings are corroborated by the EMD profiles, which provide momentum-resolved insights into the electronic states involved in positron annihilation. As shown in Fig. 4C, the momentum distribution reveals distinct peaks at approximately 10.0×10^{-3} m_0c, 16.3×10^{-3} m_0c, and 21.3×10^{-3} m_0c, corresponding to annihilation with O 2p, Ni 4s, and Cu or Ni 3d electrons, respectively.[13,51] Notably, the presence of distinct EMD features at 12.4×10^{-3} m_0c ($e_{Ni}(4s)$), 13.6×10^{-3} m_oC ($e_{Au}(5d)$), 15.6×10^{-3} m_0c ($e_{Cu}(3d)$), and 16.0–17.0 $\times 10^{-3}$ m_oC (overlapping $e_{Cu/Au}(3d/5d)$) confirms the simultaneous annihilation of positrons with both Au and Cu core electrons.[52] These characteristic signatures provide compelling evidence for the formation of an Au–Cu alloyed phase at the Ni interface, where Au and Cu atoms are chemically bonded and structurally integrated. More importantly, the low-momentum region, marked by the cyan elliptical area, corresponding to P_L below 3.5×10^{-3} m_0c, is associated with annihilation involving free or delocalized electrons. In this regime, the Au–Cu/NF sample exhibits the highest annihilation intensity, indicating a higher density of conduction electrons. This property suggests enhanced electrical conductivity due to improved electronic delocalization and enhanced charge carrier mobility. Such features are essential for promoting charge transport, which can directly contribute to the superior catalytic or photoelectrochemical performance of the Au–Cu/NF material.

Taken together, the integrated findings from PALS, DB, and EMD analyses provide a comprehensive understanding of the defect and electronic structures in the designed catalysts. The incorporation of Au not only reduces vacancy-type defects but also induces tangible modifications in the local electronic environment, as evidenced by the decrease in both positron trapping and core-electron annihilation signatures. Moreover, the enhanced annihilation in the low-momentum region reveals an increased free-electron density in the Au–Cu/NF sample, signifying improved electrical conductivity. These results may originate from the formation of an Au-based alloy, enhancing structural coherence and electronic delocalization at the atomic scale. This alloyed configuration can establish direct Au–Cu–Ni linkages, suggesting the well-integrated chemical bonding between the Au–Cu domains and the Ni foam. Such atomic-level restructuring not only facilitates more efficient solar light absorption but also significantly enhances

 This journal is © The Royal Society of Chemistry 2026

charge-transport properties. These synergistic improvements are expected to play a pivotal role in boosting the performance of the Au–Cu/NF catalyst, offering new insights into interfacial design strategies for next-generation photoelectrocatalytic systems.

The next attempts aim to explore the photoelectrochemical properties of the prepared materials for hydrogen production coupled with glucose oxidation. Fig. 5A and Fig. S4 exhibit the linear sweep voltammetry (LSV) curves of the prepared Au–Cu/NF catalyst conducted in 1.0 M KOH and in 1.0 M KOH containing 0.10 M glucose with and without light illumination. The photoelectrocatalytic glucose oxidation reaction (Pe-GOR) catalyzed by the Au–Cu/NF catalyst requires outstandingly low potentials of 0.81, 0.84, and 0.93 V *vs.* RHE to achieve currents of 10, 20, and 50 mA, respectively, which are found to be significantly lower than those of the OER counterparts. This result implies the potential of the Pe-GOR approach toward energy-saving hydrogen production. Moreover, Fig. 5B shows the LSV curves of various samples with and without irradiation. It can be said that the prepared Au–Cu/NF catalyst significantly promotes the electrocatalytic oxidation of glucose in comparison to the bare NF and Cu/NF samples, indicating the unique properties of the prepared Au–Cu/NF catalyst.

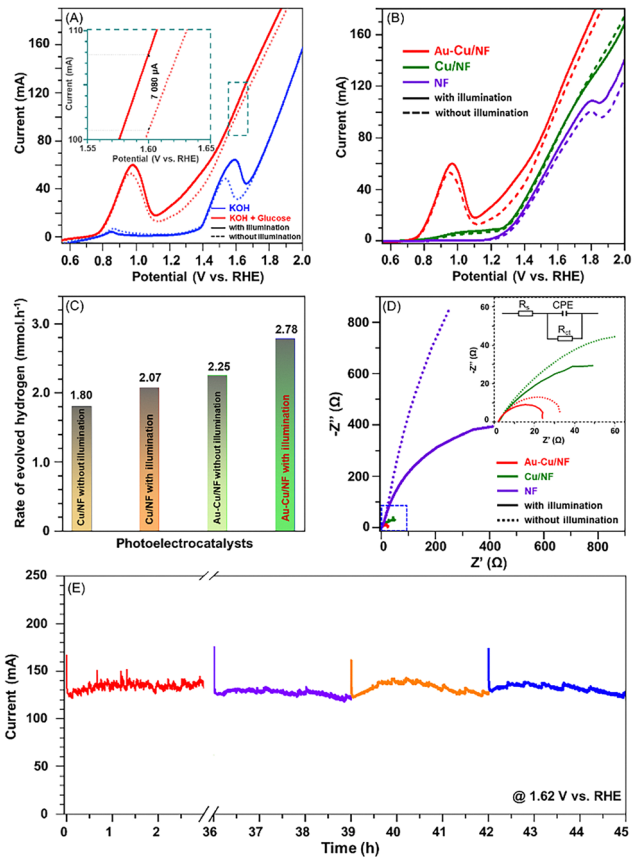

Fig. 5 LSV curves of the Au–Cu/NF sample with and without glucose (A), LSV curves (B), solar-assisted hydrogen evolution rate at the applied potential of 1.62 V *vs.* RHE (C), electrochemical impedance spectroscopy (D), and stability test (E) of the as-prepared Au–Cu/NF.

Also, Fig. 5C and Fig. S5 depict the hydrogen evolution rate of various samples measured at an applied potential of 1.62 V *vs.* RHE, which is selected to ensure a stable current for activity assessment. The absence of gas evolution at the anode during the stability test confirms the dominance of the GOR process, which is consistent with a previous report.[53] The irradiated Au–Cu/NF catalyst exhibits a H_2 production rate of ~2.8 mmol h^{-1}, which remarkably outperforms the non-illuminated Au–Cu/NF (*ca.*, 2.25 mmol h^{-1}), illuminated Cu/NF (*ca.*, 2.07 mmol h^{-1}), and non-illuminated Cu/NF (*ca.*, 1.80 mmol h^{-1}).

Fig. 5D reveals the electrochemical impedance spectroscopy (EIS) of the as-prepared materials, performed with and without solar irradiation using 1.0 M KOH and 0.10 M glucose electrolytes at an applied potential of 1.32 V *vs.* RHE. Interestingly, the Nyquist plot of the Au–Cu/NF photoelectrocatalyst shows the smallest semicircle in comparison to the rest of the samples and especially to the sample without illumination, indicating a decrease in charge-transfer resistance (R_{ct}). This observation confirms the assistance of solar light illumination, which can promote charge generation and enhance interfacial charge transport. These results provide two essential insights as follows: (i) the incorporation of Au species can significantly build a platform, promoting charge transportation, and (ii) the smallest semicircle of the solar-illuminated Au–Cu/NF catalysts implies remarkably promoted charge production and separation, which further facilitates anodic oxidation processes. Impressively, the prepared Au–Cu/NF catalyst shows outstanding stability over 45 testing hours, corresponding to an average hydrogen production rate of 2.57 mmol h^{-1} cm_{geo}^{-2}, as shown in Fig. 5E. These achievements suggest Au–Cu/NF as a robust material for solar-assisted hydrogen production coupled with glucose oxidation.

3. Conclusions

An Au-alloyed Cu/Cu_2O-decorated nickel foam photoanode is successfully prepared *via* a facile hydrothermal synthesis. The achieved material exhibits remarkable enhancement in solar light utilization and charge separation efficiencies. The employed characterizations unveil a unique structural interaction, in which the incorporation of Au atoms results in the formation of an Au–Cu alloy that directly bonds to the Ni support *via* possible Au–Cu–Ni linkages. Consequently, the prepared Au–Cu/NF photoelectrocatalyst significantly promotes performance in the solar-enhanced hydrogen production and glucose oxidation reactions. Specifically, the Au–Cu/NF sample requires low potentials of 0.81, 0.84, and 0.93 V *vs.* RHE to reach the currents of 10, 20, and 50 mA, respectively, under solar irradiation. Moreover, this material exhibits an exceptionally high amount of produced hydrogen (2.57 mmol h^{-1} cm_{geo}^{-2}) at 1.62 V *vs.* RHE and maintains stability over 15 consecutive cycles, corresponding to 45 hours of continuous operation. The presented exploration discloses a novel approach toward energy-saving solar hydrogen production.

Author contributions

Chinh Chien Nguyen: supervision, writing – original draft and editing, methodology, formal analysis, investigation. To Luong Nguyen: investigation, data curation. Do Thi Thuy Van, Trung Hieu Le, Lam Son Le: data curation. Thi Van Thi Tran, Nguyen Dang Giang Chau, Minh Khoa Duong: methodology. Minh Tuan Nguyen Dinh, Ekaterina Korneeva, Nguyen Van Tiep: resources. My Uyen Dao, Thi Hong Chuong Nguyen: Methodology, formal analysis. Anh Tuyen Luu: formal analysis, writing – review. Trong-On Do: supervision, writing – review, writing – original draft and editing.

Conflicts of interest

There are no conflicts to declare.

Data availability

The data supporting this article have been included as part of the supplementary information (SI). Supplementary information is available. See DOI: **https://doi.org/10.1039/d5tc02936h**.

Acknowledgements

The authors acknowledge the support of Hue University under the Core Research Group Program, Grant No. NCTB.DHH. 2024.09, Canada-ASEAN Development Scholarships and Laval University, Canada.

References

1 A. Odenweller and F. Ueckerdt, *Nat. Energy*, 2025, **10**, 110–123.
2 B. S. Zainal, P. J. Ker, H. Mohamed, H. C. Ong, I. Fattah, S. A. Rahman, L. D. Nghiem and T. I. Mahlia, *Renewable Sustainable Energy Rev.*, 2024, **189**, 113941.
3 S. Wei, R. Sacchi, A. Tukker, S. Suh and B. Steubing, *Energy Environ. Sci.*, 2024, **17**, 2157–2172.
4 D. Johnravindar and R. Selvakumar, *Green Hydrogen Economy for Environmental Sustainability, Volume 2: Applications, Challenges, and Policies*, American Chemical Society, 2024, ch. 1, vol. 1474, pp. 1–30.
5 L. Fei, H. Sun, Y. Li, Y. Gu, W. Zhou and Z. Shao, *Energy Environ. Sci.*, 2025, **18**, 6456–6529.
6 S. Sun, Z. Liu, Z. J. Xu and T. Wu, *Appl. Catal., B*, 2024, **358**, 124404.
7 M. P. van der Ham, J. Creus, J. H. Bitter, M. T. Koper and P. P. Pescarmona, *Chem. Rev.*, 2024, **124**, 11915–11961.
8 Y. Wu, M. Li, W. Fang, Y. Cao, S. Xin and H. Zhao, *Appl. Surf. Sci.*, 2024, **657**, 159784.
9 K. Jakubow-Piotrowska, B. Witkowski and J. Augustynski, *Commun. Chem.*, 2022, **5**, 125.
10 Q. Shi and H. Duan, *Chem. Catal.*, 2022, **2**, 3471–3496.
11 Z. Tian, Y. Da, M. Wang, X. Dou, X. Cui, J. Chen, R. Jiang, S. Xi, B. Cui, Y. Luo, H. Yang, Y. Long, Y. Xiao and W. Chen, *Nat. Commun.*, 2023, **14**, 142.
12 P. Ling, Q. Zhang, T. Cao and F. Gao, *Angew. Chem.*, 2018, **130**, 6935–6940.
13 C. C. Nguyen, C. H. N. Nguyen, T. L. Nguyen, T. H. Le, M. T. Nguyen Dinh, D. T. T. Van, H. T. Pham, H. N. T. Nguyen, T. A. Luu, N. L. Nguyen, M. U. Dao, Q. H. Nguyen, H. K. Le and Q. V. Le, *ACS Appl. Nano Mater.*, 2025, **8**, 10651–10662.
14 G. Yuan, S. Yu, J. Jie, C. Wang, Q. Li and H. Pang, *Chin. Chem. Lett.*, 2020, **31**, 1941–1945.
15 E. Alp, *Powder Technol.*, 2021, **394**, 1111–1120.
16 S. Rej, M. Bisetto, A. Naldoni and P. Fornasiero, *J. Mater. Chem. A*, 2021, **9**, 5915–5951.
17 Y. Shang and L. Guo, *Adv. Sci.*, 2015, **2**, 1500140.
18 X. Lu, L. Shen, H. Lin, L. Han, J. Du, C. Chen, J. Teng, B. Li, W. Yu and Y. Xu, *J. Hazard. Mater.*, 2024, **469**, 133973.
19 B. Zhong, S. Wan, P. Kuang, B. Cheng, L. Yu and J. Yu, *Appl. Catal., B*, 2024, **340**, 123195.
20 H.-L. Hsieh, Y.-H. Wang, C.-Y. Tsai, C.-H. Yang, E.-J. Lin and C.-C. Chen, *ACS Appl. Energy Mater.*, 2024, **7**, 8869–8881.
21 Y. Shi, Y. Li, R. Li, X. Zhao, Y. Yu and M. Yang, *Chem. Eng. J.*, 2024, **479**, 147574.
22 N. Jardón-Maximino, M. Pérez-Alvarez, R. Sierra-Ávila, C. A. Ávila-Orta, E. Jiménez-Regalado, A. M. Bello, P. González-Morones and G. Cadenas-Pliego, *J. Nanomater.*, 2018, **2018**, 9512768.
23 P. Wang, Z. Liu, C. Han, X. Ma, Z. Tong and B. Tan, *J. Nanopart. Res.*, 2021, **23**, 268.
24 G. Panzeri, M. Cristina, M. S. Jagadeesh, G. Bussetti and L. Magagnin, *Sci. Rep.*, 2020, **10**, 18730.
25 M. Zhang, J. Wang, H. Xue, J. Zhang, S. Peng, X. Han, Y. Deng and W. Hu, *Angew. Chem.*, 2020, **132**, 18621–18625.
26 W. Zhang, Y. Bai, M. Tian, Y.-G. Liu, J. Hou, C. Li, H.-Y. Jiang and J. Tang, *Adv. Mater. Interfaces*, 2023, **10**, 2201380.
27 G. Zheng, J. Wang, H. Li, Y. Li and P. Hu, *Appl. Catal., B*, 2020, **265**, 118561.
28 S. Aslam, F. Subhan, Z. Yan, A. Zada, M. Ibrahim, M. Alam, M. Yaseen and Z. Liu, *J. Mol. Liq.*, 2024, **400**, 124541.
29 A. El-Trass, H. ElShamy, I. El-Mehasseb and M. El-Kemary, *Appl. Surf. Sci.*, 2012, **258**, 2997–3001.
30 X. Zhong, Y. Zhu, Q. Sun, M. Jiang, J. Li and J. Yao, *Chem. Eng. J.*, 2022, **442**, 136156.
31 J. Huang, J. Dai, J. Zhu, R. Chen, X. Fu, H. Liu and G. Li, *J. Catal.*, 2022, **415**, 134–141.
32 Y. Yu, X. a Dong, P. Chen, Q. Geng, H. Wang, J. Li, Y. Zhou and F. Dong, *ACS Nano*, 2021, **15**, 14453–14464.
33 Y.-T. Yang, X.-H. Wang, Z.-N. Zhang, X. Ai, X. Xiao, Y. Chen and S.-N. Li, *J. Mater. Chem. A*, 2024, **12**, 29969–29977.
34 A. Yin, C. Wen, W.-L. Dai and K. Fan, *J. Mater. Chem.*, 2011, **21**, 8997–8999.
35 M. Kuhn and T. K. Sham, *Phys. Rev. B: Condens. Matter Mater. Phys.*, 1994, **49**, 1647–1661.
36 B. Bi, A.-Q. Dong, M.-M. Shi, X.-F. Sun, H.-R. Li, X. Kang, R. Gao, Z. Meng, Z.-Y. Chen, T.-W. Xu, J.-M. Yan and Q. Jiang, *Small Struct.*, 2023, **4**, 2200308.

 This journal is © The Royal Society of Chemistry 2026

37 R. Sarkar, A. A. Farghaly and I. U. Arachchige, *Chem. Mater.*, 2022, **34**, 5874–5887.

38 H. Zeng, J.-C. Chang, Y. Qu, W. Wang, J. Birch, C.-L. Hsiao and J. Sun, *Solar RRL*, 2024, **8**, 2400094.

39 M. Zhang, J. Wang, Y. Wang, J. Zhang, X. Han, Y. Chen, Y. Wang, Z. Karim, W. Hu and Y. Deng, *J. Mater. Sci. Technol.*, 2021, **62**, 119–127.

40 M. Cui, X. Ding, X. Huang, Z. Shen, T.-L. Lee, F. E. Oropeza, J. P. Hofmann, E. J. M. Hensen and K. H. L. Zhang, *Chem. Mater.*, 2019, **31**, 7618–7625.

41 B. Zhang, X. Shang, Z. Jiang, C. Song, T. Maiyalagan and Z.-J. Jiang, *ACS Appl. Energy Mater.*, 2021, **4**, 5059–5069.

42 S. Kuang, M. Li, X. Chen, H. Chi, J. Lin, Z. Hu, S. Hu, S. Zhang and X. Ma, *Chin. Chem. Lett.*, 2023, **34**, 108013.

43 S. Kuang, Y. Su, M. Li, H. Liu, H. Chuai, X. Chen, E. J. M. Hensen, T. J. Meyer, S. Zhang and X. Ma, *Proc. Natl. Acad. Sci. U. S. A.*, 2023, **120**, e2214175120.

44 L. Meng, C.-W. Kao, Z. Wang, J. Ma, P. Huang, N. Zhao, X. Zheng, M. Peng, Y.-R. Lu and Y. Tan, *Nat. Commun.*, 2024, **15**, 5999.

45 A. Hameed, F. Zulfiqar, W. Iqbal, H. Ali, S. S. Ahmad Shah and M. A. Nadeem, *RSC Adv.*, 2022, **12**, 28954–28960.

46 J. Meng, C. Hou, H. Wang, Q. Chi, Y. Gao and B. Zhu, *Nanoscale Adv.*, 2019, **1**, 2174–2179.

47 Z. Zhang, T. Cao, L. Luo, R. Song, H. Wang and W. Huang, *ChemNanoMat*, 2016, **2**, 861–865.

48 P. Phuong Ly, D.-V. Nguyen, T. Anh Luu, M. Chien Nguyen, P. Duc Minh Phan, H. Phuoc Toan, T. Van Nguyen, M.-T. Pham, T. Dieu Thi Ung, D. Danh Bich, H. Thi Pham, H. Thi Ngoc Nguyen, W. Jong Yu, S. Hyun Hur, N. Quang Hung and H.-T. Vuong, *Chem. Eng. J.*, 2025, **504**, 158657.

49 H. P. Toan, T. A. Luu, D.-V. Nguyen, M. C. Nguyen, P. D. M. Phan, N. L. Nguyen, T. Van Nguyen, L. H. Hoang, T. H. Binh, C.-L. Dong, E. Korneeva, V. H. Khoi, M.-T. Pham, T. D. T. Ung, D. D. Bich, H. T. Pham, H. T. N. Nguyen, W. J. Yu, S. H. Hur, V.-H. Dang, N. Q. Hung and H.-T. Vuong, *Small*, 2025, **21**, 2412719.

50 F. Tuomisto and I. Makkonen, *Rev. Mod. Phys.*, 2013, **85**, 1583–1631.

51 P. H. Phuoc, N. N. Viet, N. V. Chien, N. D. Cuong, N. Van Hoang, K. Lee, I. Park, P. T. Hue, N. T. Ngoc Hue, L. A. Tuyen, N. Q. Hung and N. Van Hieu, *Ceram. Int.*, 2025, **51**, 15190–15203.

52 F. H. H. Takatani, M. Nakanishi and R. Oshima, *Mater. Sci. Forum*, 2004, **445–446**, 192–194.

53 R. Crisafulli, A. de la Hoz, A. R. de la Osa, P. Sánchez and A. de Lucas-Consuegra, *ACS Sustainable Chem. Eng.*, 2025, **13**, 4963–4974.

This journal is © The Royal Society of Chemistry 2026